Scientific Reports

https://doi.org/10.1038/s41598-026-36067-3

Article in Press

Graphene-enhanced non-Hermitian Thue–Morse metamaterial sensor exploiting exceptional point for cancer biomarker detection

Received: 19 October 2025

Accepted: 9 January 2026

Published online: 28 January 2026

Cite this article as: Mohammadpour A., Vala A.S. & Barvestani J. Graphene-enhanced non-Hermitian Thue–Morse metamaterial sensor exploiting exceptional point for cancer biomarker detection. *Sci Rep* (2026). https://doi.org/10.1038/s41598-026-36067-3

Ali Mohammadpour, Ali Soltani Vala & Jamal Barvestani

Graphene-Enhanced Non-Hermitian Thue–Morse Metamaterial Sensor Exploiting Exceptional Point for Cancer Biomarker Detection

Ali Mohammadpour*, Ali Soltani Vala, Jamal Barvestani

Faculty of Physics, University of Tabriz, Tabriz 51666-16471, Iran.

**Corresponding author:* a.m.pour@tabrizu.ac.ir

Abstract. We present a one-dimensional photonic crystal biosensor based on a Thue–Morse quasi-periodic structure incorporating parity–time (PT) symmetry and exceptional point (EP) engineering for enhanced cancer detection. By integrating alternating porous silicon gain–loss layers with graphene nanolayers, the proposed design achieves strong optical confinement and pronounced resonance sharpening near EP conditions. A systematic parametric study identified the optimal graphene chemical potential and relaxation time as 0.408 eV and 0.5 ps, respectively, leading to a maximum sensitivity of 1054 nm/RIU and a minimum detection limit of 9.875×10^{-4} RIU. Moreover, the analysis reveals that increasing the number of graphene layers results in a progressive enhancement in sensitivity accompanied by a reduction in the optimal porosity percentage, highlighting the strong influence of graphene-induced field confinement on device performance. These results surpass those of conventional one-dimensional biosensors, demonstrating the combined advantages of PT symmetry and graphene-assisted field enhancement. Fabrication tolerance analysis confirmed the structural robustness, underscoring its potential for practical implementation. Overall, the findings establish PT-symmetric Thue–Morse photonic crystals as a versatile platform for ultra-sensitive, label-free biomedical sensing, paving the way for next-generation optical diagnostic technologies.

Keywords. Cancer cells, Exceptional points, Graphene, Parity-time symmetry, Refractive index, Sensitivity, Thue-Morse sequence.

1. Introduction

Early, label-free, and high-sensitivity detection of cancer cells and biomarkers is a continuing priority for biomedical diagnostics and point-of-care testing. Optical biosensors built from engineered photonic structures especially one-dimensional (1D) photonic crystals (PhCs) are attractive because their layered geometries offer strong field confinement, easily measurable spectral signatures (resonances, reflection/transmission features), and straightforward integration with silicon-based fabrication and microfluidics. Defect modes introduced into 1D PhCs produce narrow, highly localised resonances whose spectral position is susceptible to changes of the local refractive index, a property widely exploited in optical biosensing [1, 2]. Recent progress in plasmonic and photonic biosensing has led to the development of a broad class of high-performance SPR-based sensor configurations. Several recent studies have demonstrated that integrating SPR with specially-engineered photonic crystal fibers (PCFs), kagome-lattice hollow-core structures, and external-metal-deposition geometries can significantly enhance refractive-index sensing performance for a wide range of biological and chemical analytes. For instance, hollow-core kagome PCF-SPR sensors have achieved extremely high wavelength sensitivities for blood-related biomarkers under dual-polarization excitation. Comprehensive reviews of PCF-SPR architectures further highlight their versatility, structural tunability, and ability to detect biomolecules such as glucose, cholesterol, DNA, proteins, and cancer cells with improved field confinement and plasmonic interaction strength. Recent designs using square-lattice PCFs with external metal deposition have also achieved high sensitivity and demonstrated strong linearity and robust operation in complex sensing environments, with emerging directions incorporating machine-learning-assisted optimization. In parallel, optical biosensing technologies, including SPR, LSPR, Raman-based sensors, photonic-waveguide platforms, and fiber-optic configurations have been extensively employed for cancer biomarker detection owing to their high precision, label-free operation, and real-time capability [3, 4, 5, 6, 7, 8]. These developments collectively underline the rapid evolution of SPR and photonic-crystal-based biosensors and motivate the pursuit of advanced hybrid architectures, such as PT-symmetric and graphene-assisted systems, capable of surpassing the sensitivity and spectral performance of conventional SPR-only approaches.

Meanwhile, two directions in photonic design provide prosperous opportunities to enhance sensitivity. First, non-Hermitian photonics with balanced gain and loss that satisfy parity–time (PT) symmetry can generate exceptional points (EPs) non-Hermitian degeneracies where eigenvalues and eigenvectors coalesce and operation near EPs can strongly amplify a system's spectral response to small perturbations [9, 10]. This principle has been demonstrated theoretically and experimentally across cavity, waveguide, and resonator platforms and has been proposed as a route to EP-enhanced sensing. At the same time, recent analyses emphasize practical tradeoffs (noise amplification, stability, and realistic gain/loss engineering) that must be addressed for EP sensing to deliver robust improvements in signal-to-noise ratio [11]. Second, quasi-periodic sequences such as the Thue–Morse (ThM) order occupy an intermediate design space between perfect periodicity and disorder. ThM-ordered multilayers and quasicrystals exhibit multiscale, self-similar spectral features and localized states that can produce narrow resonances without a simple Bragg periodicity. These properties make ThM structures appealing for multi-channel sensing and for engineering localized field enhancements around defect layers. Prior theoretical

and experimental studies have shown that ThM and related quasi-periodic sequences can support sharp spectral features and valuable localization for sensing and filtering applications [12, 13].

Materials engineering of the defect (analyte) layer further improves transduction. Porous silicon (PSi) is a mature material platform for optical biosensing because its effective refractive index and pore architecture are tunable via electrochemical etching, it provides an extensive internal surface area for biochemical functionalization, and it allows direct infiltration of liquid analytes (cells, proteins, or suspensions) into the sensing volume. PSi-based Bragg stacks, microcavities, and rugate filters have been demonstrated for label-free detection of bacteria, proteins, and cellular suspensions; recent reviews summarize fabrication, surface chemistry, and optimization strategies for PSi biosensors [14]. In addition, graphene and graphene-derived nanolayers have emerged as powerful additives in optical sensors because of their exceptional optical, electrical, and surface-chemistry properties. A single or few layers of graphene coupled to photonic structures (e.g., plasmonic films, Bloch surface waves, or PhCs) can increase light–matter interaction, provide strong broadband absorption/tunable dispersion, and serve as a robust chemical or biological functionalization platform that improves analyte capture and device stability. Several studies have successfully integrated graphene nanolayers with photonic crystals and surface-plasmon sensors to demonstrate enhanced sensitivity and lower detection limits for biomolecules and cells [15, 16, 17, 18, 19]. Compared with conventional PRISM-SPR sensors that rely on noble-metal films with high intrinsic damping, graphene provides electrically tunable optical conductivity, lower plasmonic losses, and stronger near-field confinement. These advantages enable sharper resonances and improved detection limits, particularly when combined with PT-symmetry and exceptional-point engineering.

Accordingly, a one-dimensional PhC organized by a Thue–Morse sequence, and also PT-symmetric gain–loss engineering to create and operate near EPs, and the optional integration of graphene nanolayers to enhance light-matter coupling besides porous silicon mediums creates a rich design space for next-generation biosensors aimed at cancer-cell detection. Each component contributes complementary advantages: ThM ordering supplies multiscale localized spectral states that can be tuned to overlap with defect resonances; PT symmetry or EP physics offers parametric amplification of perturbation responses; PSi provides direct analyte infiltration and high surface area; and graphene layers improve optical coupling and biochemical functionalization [20, 21, 22, 23, 24, 25, 26, 27]. Prior works establish the viability of the individual components EP-enhanced sensing in microcavities and silicon resonators, ThM-based photonic devices with sharp localized modes, PSi biosensors with tunable effective index, and graphene-assisted photonic biosensors but integrated devices that combine aforementioned elements remain largely unexplored. The quasi-periodic Thue–Morse arrangement provides distinct optical properties that cannot be obtained from conventional periodic photonic-crystal structures. In a periodic Bragg-type multilayer, the resonant modes are primarily determined by regular bandgap dispersion and exhibit limited field localization, resulting in resonances with moderate sharpness. In contrast, the ThM sequence generates a self-similar spectral response that supports critical modes lying between fully extended and fully localized states. These critical modes exhibit strong near-field confinement within specific quasi-defect regions of the ThM stack and significantly reduced radiative leakage compared with periodic structures, thereby producing much sharper resonances with smaller FWHM. Furthermore, the enhanced localization at the sensing interface increases the overlap between the optical field and the analyte layer, leading to a larger spectral shift for a given

refractive-index perturbation. Consequently, the ThM-based architecture provides simultaneously stronger field confinement and steeper resonance slopes than periodic multilayers, explaining the superior sensitivity demonstrated in our design. These features underline the advantage of employing quasi-periodicity for high-performance refractive-index biosensing.

In this work we propose and analyze a 1D Thue–Morse photonic crystal incorporating a central analyte defect layer and porous silicon layers encompassed by gain/loss elements that realize PT symmetry. We further investigate the presence and absence of graphene nanolayers placed at selected interfaces. Using transfer-matrix methods, non-Hermitian eigenanalysis, and parametric optimization, we identify defect-mode resonances and map exceptional points as a function of the refractive indices of analyte. Next, quantify biosensor performance via wavelength-shift sensitivity and limit of detection metrics while accounting for realistic material dispersion and loss, and considering the fabrication tolerance, the structure-dependent parameters are improved and the optimal values are reported. Our results show that the combined strategy ThM ordering, PSi mediums, controlled PT symmetry, and optionally augmented with graphene nanolayers provides a flexible platform for high-sensitivity, label-free cancer-cell detection, and they identify design rules that balance sensitivity enhancement with experimental feasibility. The performance metrics obtained in this study are highly competitive compared to previously reported one-dimensional photonic biosensors. Conventional multilayer structures typically exhibit sensitivities in the range of 200–600 nm/RIU with detection limits on the order of 10^{-3}–10^{-4} RIU. More advanced configurations, such as defect-based or topological photonic crystals, and fiber-integrated designs can achieve even higher sensitivities, but often at the expense of increased fabrication complexity and reduced compactness. In contrast, the proposed PT-symmetric nanophotonic biosensor incorporating graphene demonstrates a sensitivity of 1054 nm/RIU with a detection limit of 9.875×10^{-4} RIU under the initial design parameters, and significantly enhanced performance under optimized conditions. These improvements highlight the critical role of graphene integration and exceptional point engineering in simultaneously achieving miniaturization, high sensitivity, and low detection limits, thereby offering a robust platform for practical cancer and tissue diagnostics in exact Thue-Morse configuration. The synergy between field enhancement from graphene and loss compensation through PT symmetry results in a robust sensing platform capable of detecting low-abundance cancer biomarkers with high precision. This combination ensures that the biosensor operates effectively in real-time applications, providing reliable and sensitive diagnostics.

The remainder of the paper is organized as follows. Section 2 describes the device geometry and theoretical approaches. Section 3 presents spectral results, EP mapping, and sensitivity maps for structures with and without graphene layers. Besides, discusses optimization outcomes, and stability considerations. Section 4 concludes.

2. Methods and Theoretical Approach

The proposed device is a one-dimensional (1D) photonic crystal composed of alternating dielectric layers arranged according to a Thue–Morse (ThM) sequence. The ThM sequence is generated recursively from two building blocks A and B, where A and B correspond to dielectric layers of distinct refractive indices. The primary generation begins with A; the first is obtained by substituting A→AB, B→BA; higher orders are constructed iteratively [28]. This deterministic quasi-periodic sequence produces spectral features with self-similar transmission bands. A central defect layer is introduced by replacing one ThM unit with an investigated analyte layer (e.g., buffer solution or cancer-cell suspension). Gain and loss are introduced into selected alternating layers to satisfy the parity–time (PT) symmetry condition, where the real part of the refractive index is even and the imaginary part (associated with optical gain or loss) is odd with respect to the structure's center.

In some configurations, single or multiple graphene nanolayers are inserted at the interfaces between dielectric layers, especially adjacent to the defect layer, to enhance optical field confinement and light–matter interaction. Graphene is modeled as a two-dimensional (2D) conductive sheet of negligible thickness, characterized by a surface conductivity $\sigma(\omega)$. The optical response is included in the transfer-matrix method as a boundary condition at the graphene-containing interface. The complex conductivity is described by the Kubo formula [29, 30], which accounts for both interband and intraband transitions:

$$\sigma(\omega)=\sigma^{inter}(\omega)+\sigma^{intra}(\omega)\rightarrow\begin{cases}\sigma^{inter}(\omega)=i\dfrac{e^2}{4\pi\hbar}\ln\left[\dfrac{2|\mu_c|-\hbar(\omega+i\tau^{-1})}{2|\mu_c|+\hbar(\omega+i\tau^{-1})}\right]\\ \sigma^{intra}(\omega)=i\dfrac{e^2k_BT}{\pi\hbar^2(\omega+i\tau^{-1})}\left[\dfrac{\mu_c}{k_BT}+2\ln\left(\exp\left(-\dfrac{\mu_c}{k_BT}\right)+1\right)\right]\end{cases} \quad (1)$$

where μ_c is the chemical potential (tunable via electrostatic gating or chemical doping). Parameters τ, k_B represents the relaxation time and Boltzmann's constant, respectively. The parameter T is the temperature. Also $\hbar = h/2\pi$, is reduced Planck's constant, and e is the electronic charge.

The optical response of the multilayer system is calculated using the transfer-matrix method (TMM) [31]. For each layer j of thickness d_j, refractive index n_j, and wavevector $k_j = 2\pi n_j/\lambda$, the propagation matrix is:

$$P_j=\begin{pmatrix}e^{ik_jd_j} & 0\\ 0 & e^{-ik_jd_j}\end{pmatrix} \quad (2)$$

At each interface (with or without graphene), boundary matrices I_j are constructed from the Fresnel coefficients [32]. The total transfer matrix is: $M = \prod_{j=1}^{N} I_j P_j$, and the transmittance spectrum is obtained from [33]:

$$T_{b(f)}(\lambda) = \left|t_{b(f)}\right|^2 = \frac{n_s}{n_0}\frac{1}{\left|M_{11}\right|^2} \;;\; R_b(\lambda) = \left|r_b\right|^2 = -\frac{n_s}{n_0}\frac{\left|M_{21}\right|^2}{\left|M_{11}\right|^2} \;;\; R_f(\lambda) = \left|r_f\right|^2 = \frac{n_s}{n_0}\frac{\left|M_{12}\right|^2}{\left|M_{11}\right|^2} \quad (3)$$

where n_0 and n_s are the refractive indices of the incident and substrate media, respectively. The scattering behavior of incident and scattered waves can be described by a scattering matrix $S = [t_b\ r_f; r_b\ t_f]$. The corresponding eigenvalues can be derived from $\beta_{1,2} = t_{b(f)} \pm \sqrt{r_b r_f}$, equation. According to the conservation relation for spectra $R_b R_f = (T_{b(f)}-1)^2$, when the transmissivity is unitary, the two eigenvalues coalesce at $\sqrt{r_b r_f} = 0$, and the reflectivity is zero which approving phase transition point and the exceptional points (EPs) occur. At the exceptional point, both eigenvalues and eigenvectors of the scattering matrix coalesce, leading to a non-Hermitian degeneracy that strongly amplifies the spectral response to perturbations. EPs play a crucial role in understanding the transitions between PT-symmetric and broken PT-symmetric phases. For PT-symmetric analysis, the imaginary part of n_j is adjusted to represent optical gain and loss, while maintaining the parity-time symmetry condition $n(r)=n^*(-r)$. The refractive indices of the gain and loss layers, where silica is employed as the host medium doped with quantum dots, can be described by the Lorentzian dispersion model [34]:

$$\varepsilon(\omega) = \varepsilon_h + \frac{\alpha_{G(L)}\omega_p^2}{\omega_0^2 - \omega^2 - i\gamma\omega} \quad (4)$$

where ε_h=1.5 is the background permittivity of the host material (silica), and the second term represents the macroscopic Lorentz oscillation of the quantum-dot-doped layers. In this expression, $\omega_0 = 1.216\times10^{15}$ rad/s, is the resonance frequency, ω is the angular frequency of the incident wave, and $\gamma = 2.5\times10^{14}$ s^{-1}, denotes the damping factor. The parameter $\alpha_{G(L)}$ represents the related macroscopic Lorentz oscillation of the gain and loss layer, and ω_p is the effective plasma frequency associated with the quantum dot excitation. Exceptional points (EPs) are identified by tracking eigenvalue coalescence of the transfer matrix or by monitoring resonance splitting behavior as a function of the gain/loss parameter.

The refractive index of porous silicon is calculated by Bruggeman's effective medium approximation [16]:

$$n_{PSi} = 0.5\left(\Omega + \sqrt{\Omega^2 + 8n_{Si}^2 n_{sample}^2}\right)^{\frac{1}{2}} \quad (5)$$

Where $\Omega = 3P\left(n_{sample}^2 - n_{Si}^2\right) + \left(2n_{Si}^2 - n_{sample}^2\right)$, and P, n_{sample}, n_{Si} are the porosity ratio and refractive indices of the analyte sample and silicon, respectively.

The primary performance metrics are sensitivity (S) and limit of detection (LoD), defined as [35]:

$$S(nm/RIU) = \frac{\Delta\lambda_m}{\Delta n_s}$$
$$LoD(RIU) = \frac{FWHM}{20S} \quad (6)$$

where $\Delta\lambda_m$ is the resonance wavelength shift per unit change in analyte refractive index Δn_s. The parameter FWHM is the full width at half maximum of the resonance. To quantify the sensing performance of the proposed structure, the resonance wavelength, full width at half maximum (FWHM), and the resulting detection limit (LoD) were evaluated using the following procedure. For each refractive index value of the analyte, the transmission spectrum was computed across the wavelength range of interest. The resonance wavelength was defined as the location of the maximum (for transmission peaks T) of the spectral feature. The FWHM was obtained directly from the resonance curve. First, the resonance amplitude was identified, then the half-maximum value was computed (T_{half}). The two wavelengths λ_1 and λ_2 where ($T(\lambda_1)=T(\lambda_2)=T_{half}$), were found by interpolation, and the FWHM was calculated ($FWHM=|\lambda_2 - \lambda_1|$). The narrowing of the resonance near the exceptional point therefore naturally manifests as a reduced FWHM.

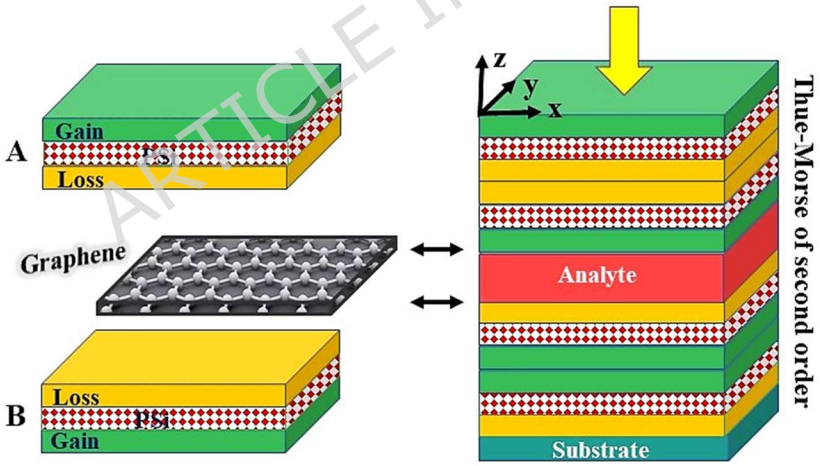

Figure 1. Schematic illustration of the one-dimensional Thue–Morse photonic crystal incorporating a central analyte layer for cancer biosensing applications. Red dotted layers indicate porous silicon.

3. Results and Discussion

For the structure illustrated in Fig. 1, the transmission spectrum and the phase variations of the reflected wave under normal electromagnetic incidence are presented in Fig. 2. The occurrence of

a phase jump of π radians, together with the corresponding eigenvalues of the scattering matrix, enables the identification of exceptional points (EPs). Accordingly, the structural parameters were optimized based on the locations of these EPs. In this configuration, the thicknesses of the gain and loss layers are 400 nm, the sample layer is 2000 nm, and the porous layers (with 30% porosity) are 172 nm thick. A graphene monolayer of 0.34 nm is deposited on both sides of the sample layer. The macroscopic Lorentz oscillation intensity for the gain and loss layers are set to -2.3×10^{-4} and 2.3×10^{-4}, respectively. Comprehensive parameter specifications, including all details necessary for repeatability and further investigation of the biosensor design and performance, are summarized in Table 1.

Table 1. Comprehensive list of parameters used in the biosensor design, providing all necessary details for accurate modeling and reproducibility.

Parameter	symbol	Initial value	Description
Refractive index of analyte (sample)	n_s	1.350	For healthy cell.
		1.380-1.401	For cancerous cells: 1.380, 1.390, 1.392, 1395, 1.399, 1401.
Thickness of Gain/Loss layers	$d_{G/L}$	400 nm	Thickness of alternating gain and loss with negative and positive in imaginary part of refractive indices.
Thickness of porous silicon layers	d_P	172 nm	Thickness of the porous silicon layers, which provide a high surface area for analyte interaction.
Thickness of the sample layer	d_S	2000 nm	Thickness of the analyte (e.g., cancer cell suspension or buffer solution) layer where detection occurs.
Porosity of porous silicon layers	P	30 %	Percentage of porosity in the porous silicon layers, affecting the refractive index and analyte infiltration.
Macroscopic Lorentz oscillation intensity	α	$\pm2.3\times10^{-4}$	The macroscopic Lorentz oscillation intensity for the gain and loss layers.
Incident angle	θ	0°	The incident angle of EMW to the structure.
Chemical potential of graphene	μ_c	0.4 eV	Tunable via electrostatic gating or chemical doping; influences graphene conductivity and sensor sensitivity.
Relaxation time of graphene	τ	0.4 ps	Represents carrier dynamics in graphene; affects the damping of plasmonic modes and sensitivity.
Background permittivity of silica	ε_h	1.5	The permittivity of the host medium (silica) used in the structure.
Damping factor	γ	2.5×10^{14} S^{-1}	Damping coefficient used in the Lorentzian model for gain/loss layers.
Resonance frequency	ω_p	1.216×10^{15} rad/s	Characteristic frequency for the Lorentzian dispersion model of the gain/loss layers.
Thickness of graphene layer	d_g	0.34 nm	Thickness of each graphene layer.
Temperature	T	300 K	The maintaining temperature of system.

The refractive indices of the sample layer, corresponding to healthy and cancerous cells, are 1.350, 1.380, 1.390, 1.392, 1.395, 1.399, and 1.401. As shown in Fig. 2, the photonic band gap lies in the spectral range of approximately 1360–1790 nm. In the presence of graphene, the maximum transmission for the healthy-cell case occurs at 1550 nm with an amplitude of 1.77, whereas in the absence of graphene, the maximum transmission reaches only unity.

Meanwhile, operating the Thue–Morse PT-symmetric photonic crystal exactly at the EP induces a characteristic square root dependence of the eigenvalue splitting on refractive-index perturbations,

resulting in an asymmetric and sharply varying resonance profile with a considerably reduced FWHM. Consequently, the minimum detectable wavelength shift decreases while the effective sensitivity increases from the below-EP value to its maximum at the EP, further confirming the crucial role of EP engineering in boosting the sensing performance of the proposed structure.

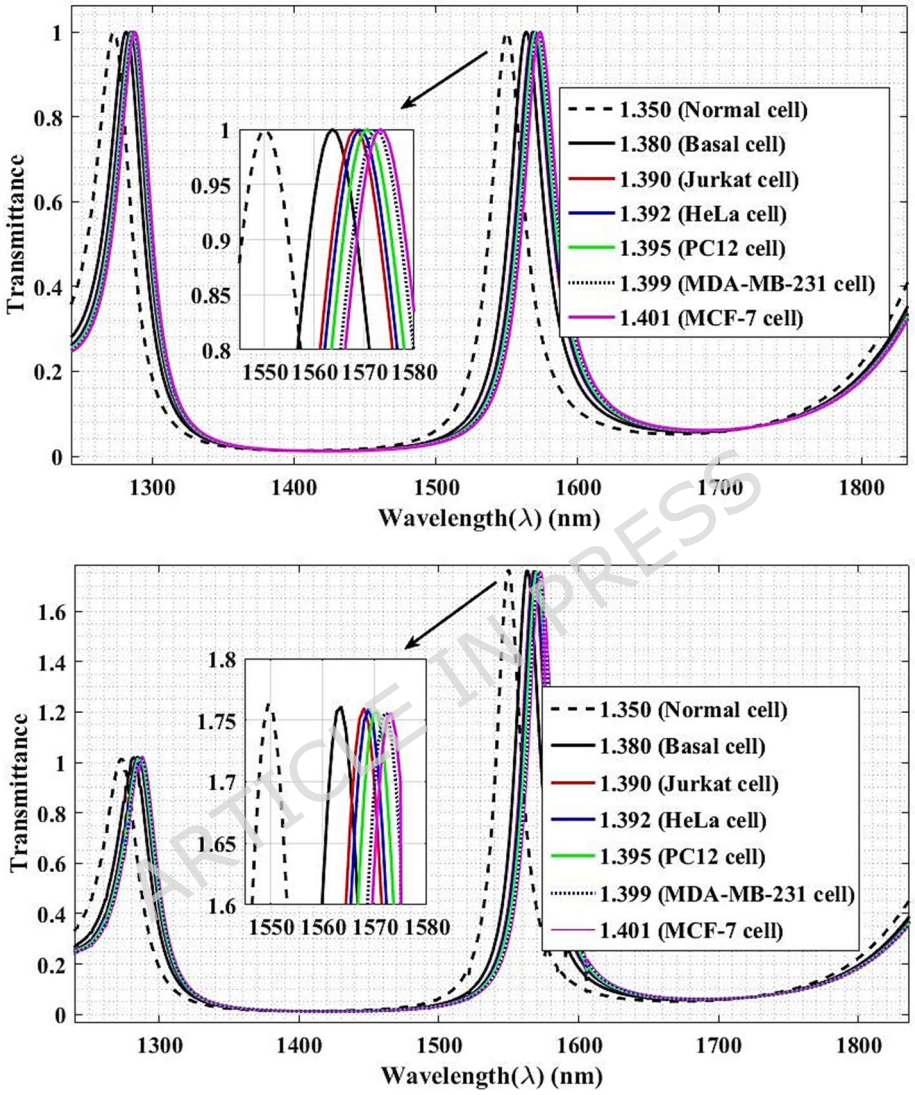

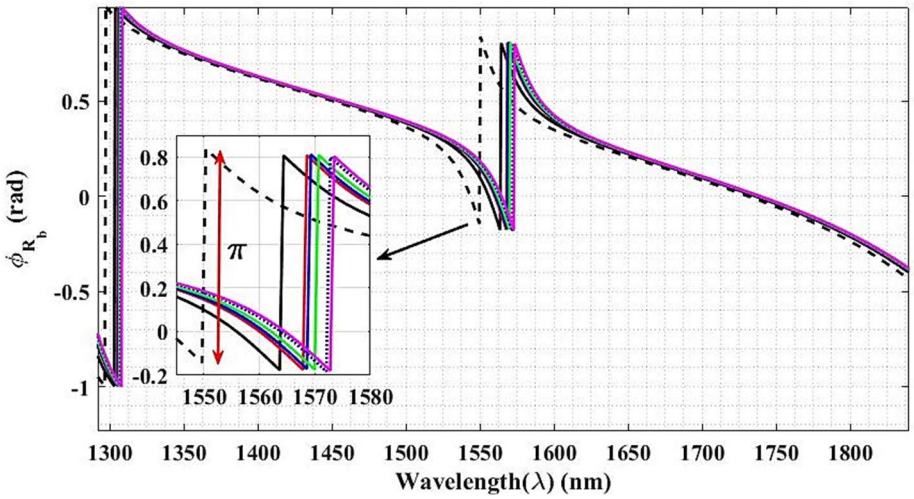

Figure 2. Transmittance spectra for the structure without graphene (top) and with graphene (middle), along with the phase variations of the backward reflection for both cases (bottom). The insets present magnified regions.

At the resonance wavelength λ=1550 nm, we calculated the transmission, reflection, and reflection phase as functions of the sample refractive index, as shown in Fig. 3. A clear EP is observed at n_s=1.350, where the transmittance equals one, while the reflectance components are simultaneously equal to zero. Notably, the reflection phase exhibits a π-phase jump and the two eigenvalues of the scattering matrix coalesce. This coalescence is the hallmark of EP physics and is accompanied by an abrupt change in the resonance slope of the transmission spectrum. Such a steepening of the spectral response near the EP significantly enhances the refractive-index sensitivity because even a minute change in the sample refractive index produces a disproportionately large wavelength shift. This behavior is consistently observed at each EP corresponding to the resonance wavelengths associated with the refractive indices of cancerous cells.

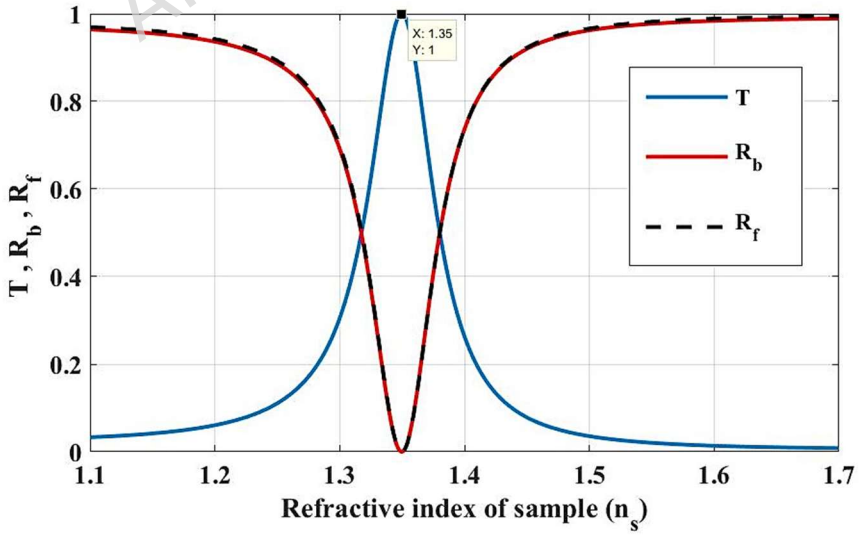

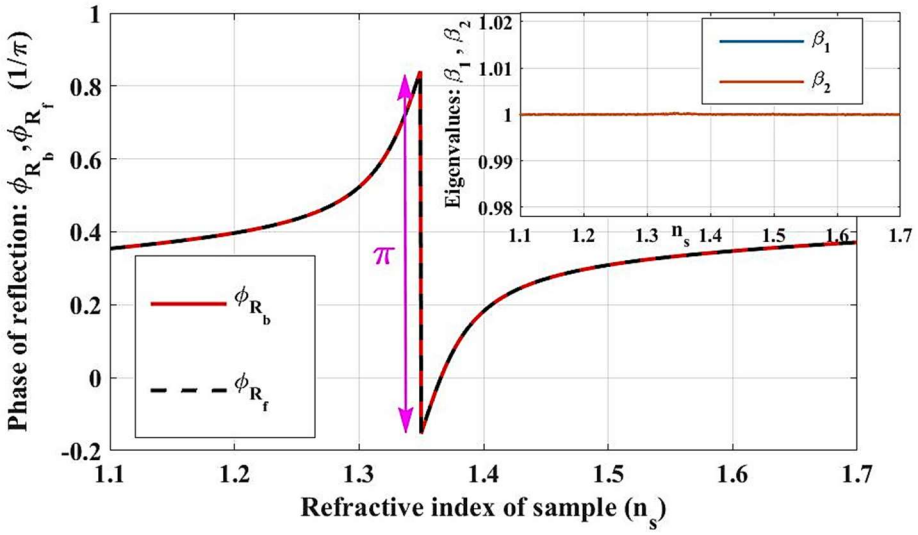

Figure 3. Transmittance and backward/forward reflectance (top), and the corresponding phase variations of the backward/forward reflectance (bottom) as functions of the sample refractive index. The inset presents the evolution of the scattering-matrix eigenvalues, highlighting their coalescence at the exceptional point.

To assess the robustness of the proposed sensor, we systematically investigated the impact of fabrication tolerances on its sensing performance. Most structural parameters were evaluated within a variation range of ±2%. Accordingly, structural deviations were analyzed in terms of their stability ranges, and the corresponding sensitivity and detection limit values were calculated.

Figure 4 illustrates the variation of sensitivity with respect to layer thicknesses: (i) the gain and loss layers varied from 392 to 408 nm (top panel), (ii) the porous layers varied from 168 to 176 nm (middle panel), and (iii) the sample layer varied from 1950 to 2040 nm (bottom panel). Each case was examined in the presence and absence of the graphene layer to highlight its influence. The chemical potential and relaxation time of graphene were set to 0.4 eV and 0.4 ps, respectively, with the system temperature maintained at 300 K. The results show that while there are some fluctuations in sensitivity due to these tolerances, the overall performance remains robust within the specified range.

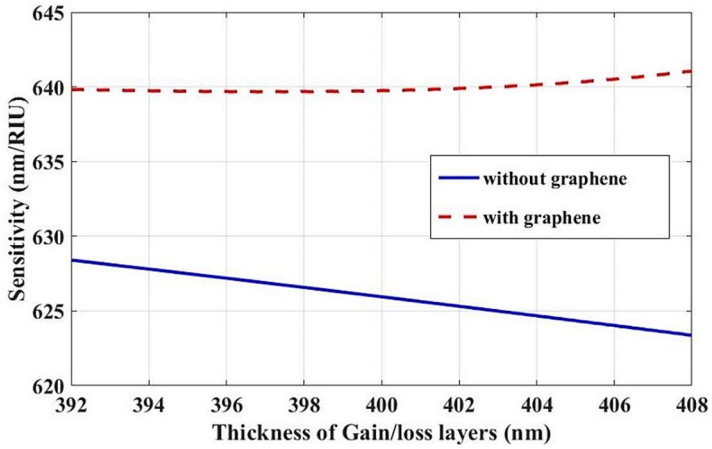

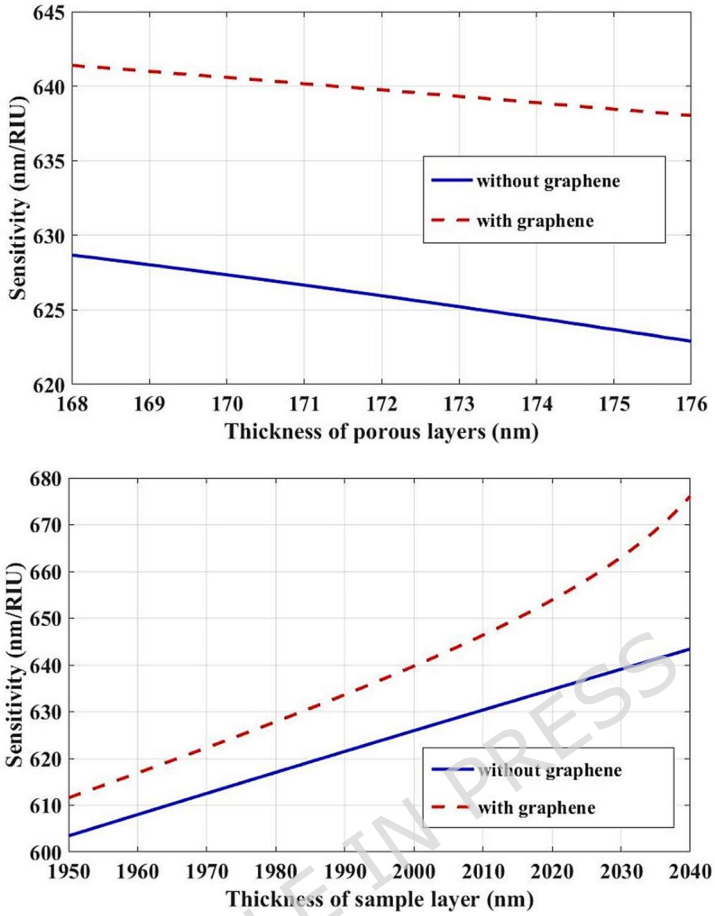

Figure 4. Sensitivity as a function of the thickness of the gain/loss layers (top), the porosity layers (middle), and the sample layer (bottom), evaluated within the specified tolerance range.

Figure 5 presents the sensitivity as a function of three key parameters: porosity percentage (top), macroscopic Lorentzian oscillation intensity (middle), and incident angle (bottom). Where transverse electric (TE) polarization is taken into account. The results reveal a clear trend of increasing sensitivity with larger values of these structure-dependent parameters. Significantly, the incorporation of graphene consistently enhances the sensitivity compared to the graphene-free configuration.

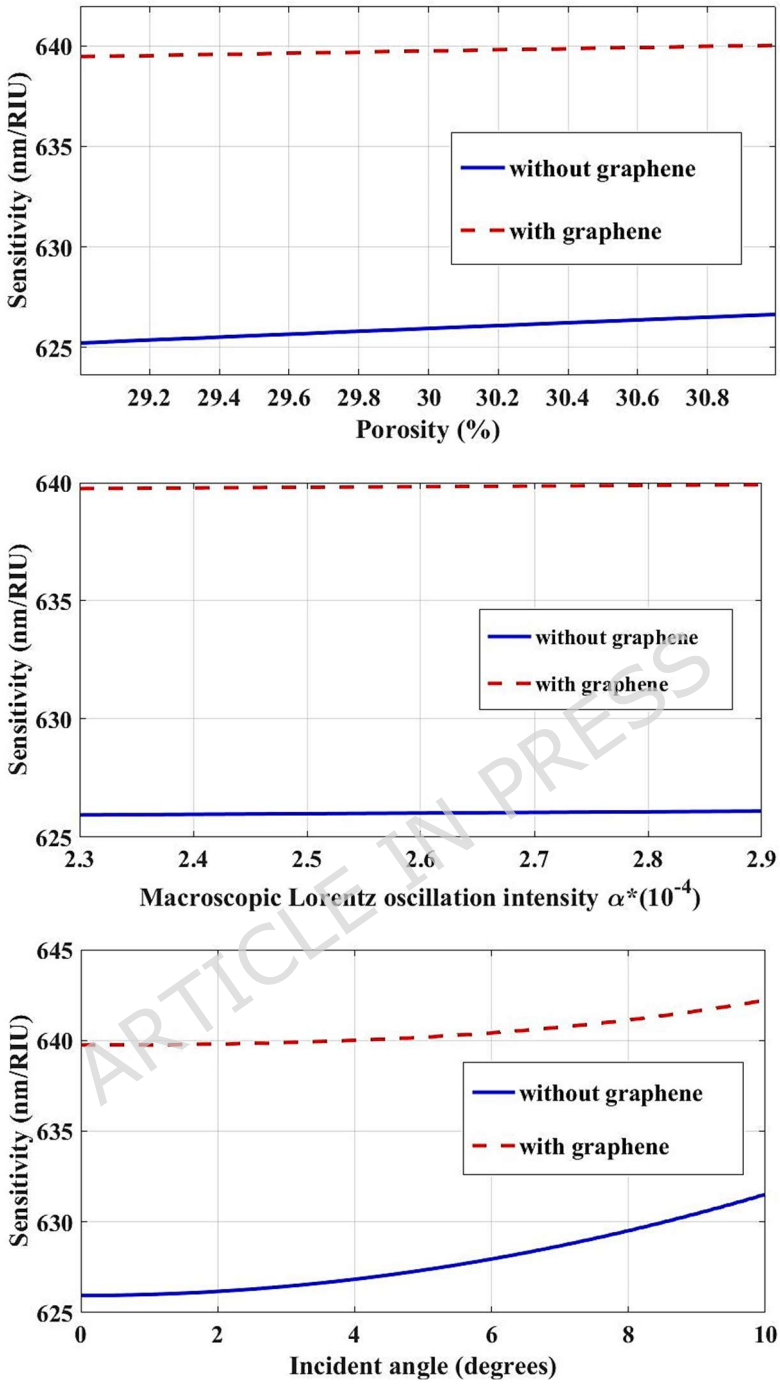

Figure 5. Sensitivity as a function of porosity (top), macroscopic Lorentz oscillation intensity (middle), and incident angle (bottom), evaluated within the tolerance range.

Figure 6 illustrates the sensitivity analysis as a function of layer thickness variations within the fabrication tolerance range for different values of the graphene chemical potential. The results show that, at a chemical potential of 0.408 eV, the sensitivity significantly increases and reaches its maximum at the initially designed thickness values. This enhancement is consistently observed

across all three investigated thickness parameters, highlighting the critical role of graphene's chemical potential in optimizing the sensor's performance.

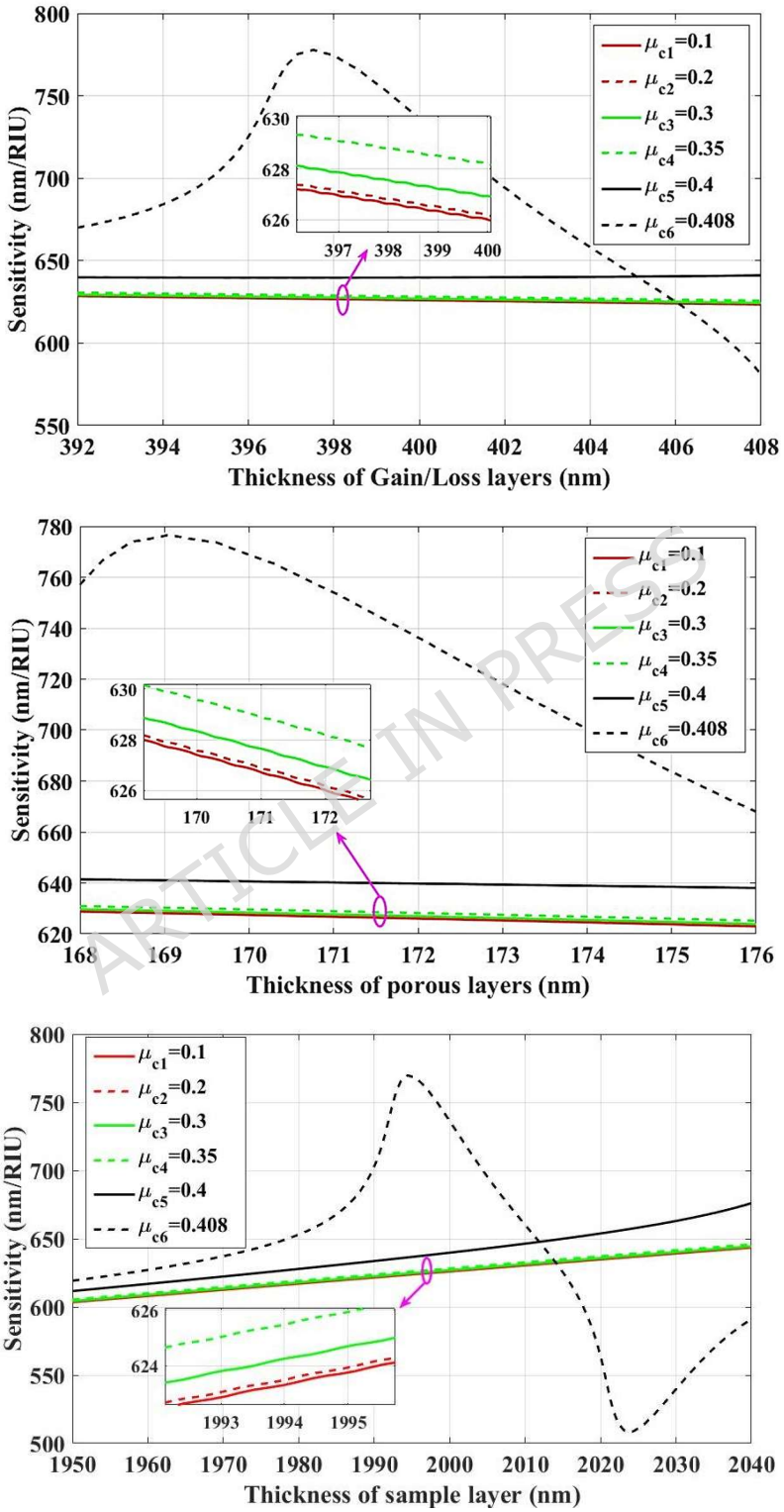

Figure 6. Sensitivity versus the thicknesses of gain(loss) layers (up), porosity layers (middle), and sample layer (down), within the tolerance range for various chemical potentials.

Figure 7 presents the sensitivity as a function of porosity, macroscopic Lorentz oscillation intensity, and incidence angle for different values of graphene chemical potential. In the upper panel, the sensitivity remains nearly constant with increasing porosity for most chemical potentials; however, at $\mu_c = 0.408$ eV, the sensitivity exhibits a pronounced increase as porosity rises. In contrast, variations in the Lorentz oscillation intensity produce little change in sensitivity, although the middle panel shows that higher chemical potentials generally enhance sensitivity, reaching a maximum at $\mu_c = 0.408$ eV. A similar trend is observed for the incidence angle in the lower panel, where sensitivity increases with chemical potential and peaks at $\mu_c = 0.408$ eV.

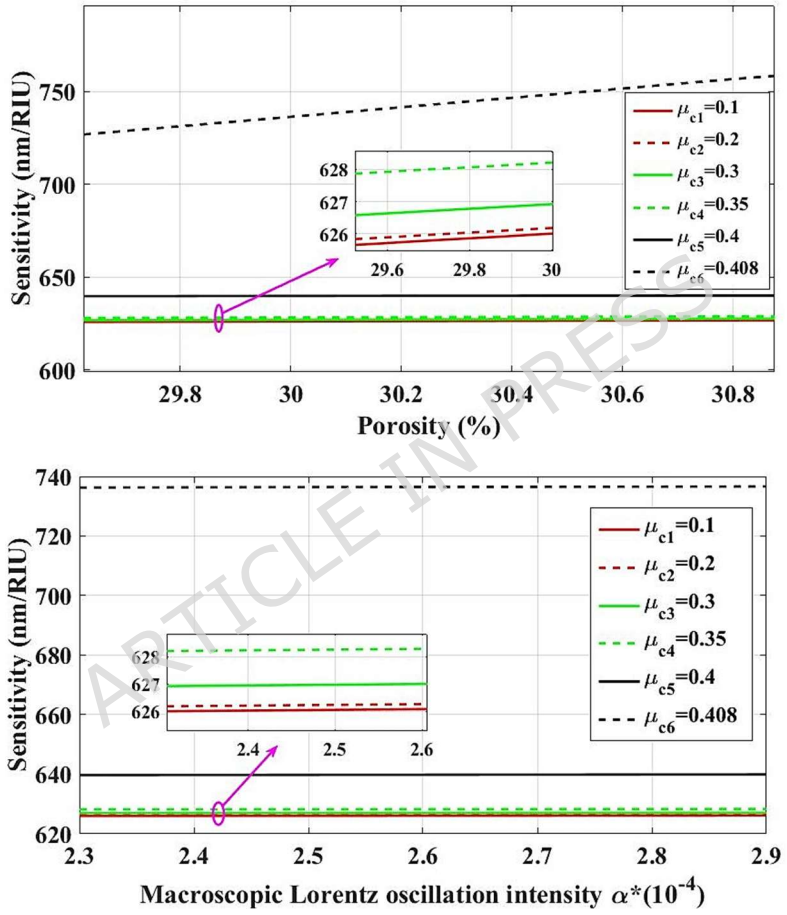

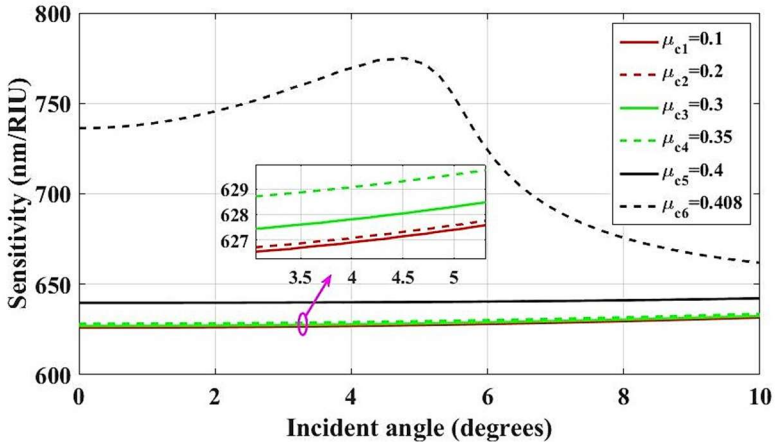

Figure 7. Sensitivity as a function of porosity (top), macroscopic Lorentz oscillation intensity (middle), and incident angle (bottom), evaluated within the tolerance range for different chemical potentials.

For a chemical potential of 0.408 eV, the influence of relaxation time on the structure-dependent parameters is illustrated in Figures 8 and 9. Figure 8 depicts the variations associated with layer thicknesses. As the relaxation time increases, the sensitivity consistently improves across all thickness variations, reaching its maximum at a relaxation time of 0.5 ps. Notably, with increasing relaxation time, the peak sensitivity values shift toward smaller thicknesses, indicating a strong interplay between temporal carrier dynamics and structural optimization.

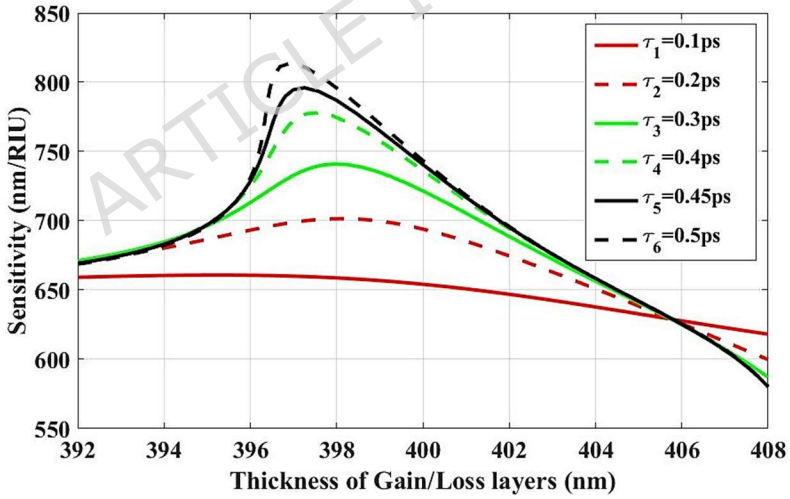

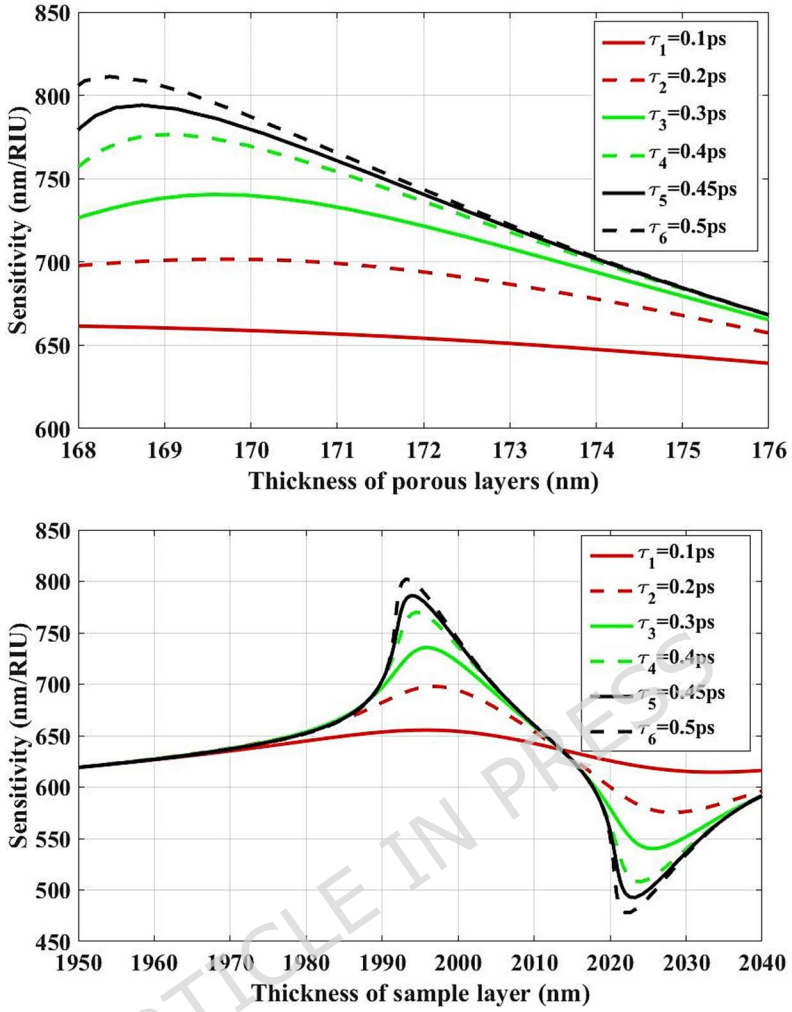

Figure 8. Sensitivity as a function of the thicknesses of the gain (loss) layers (top), porosity layers (middle), and sample layer (bottom), evaluated within the tolerance range for different relaxation times.

Figure 9 illustrates the effect of relaxation time on the sensor's sensitivity for different structural parameters. In the top panel, sensitivity increases with both relaxation time and porosity, with the highest value observed at τ = 0.5 ps. The middle panel shows that sensitivity remains largely unaffected by variations in the Lorentz oscillation intensity, while it still increases with longer relaxation times. In the bottom panel, the sensitivity as a function of incidence angle reveals that the peak shifts toward larger angles as the relaxation time increases, reaching its maximum at τ = 0.5 ps. These results highlight the significant role of relaxation time in optimizing the sensor performance across multiple structural parameters.

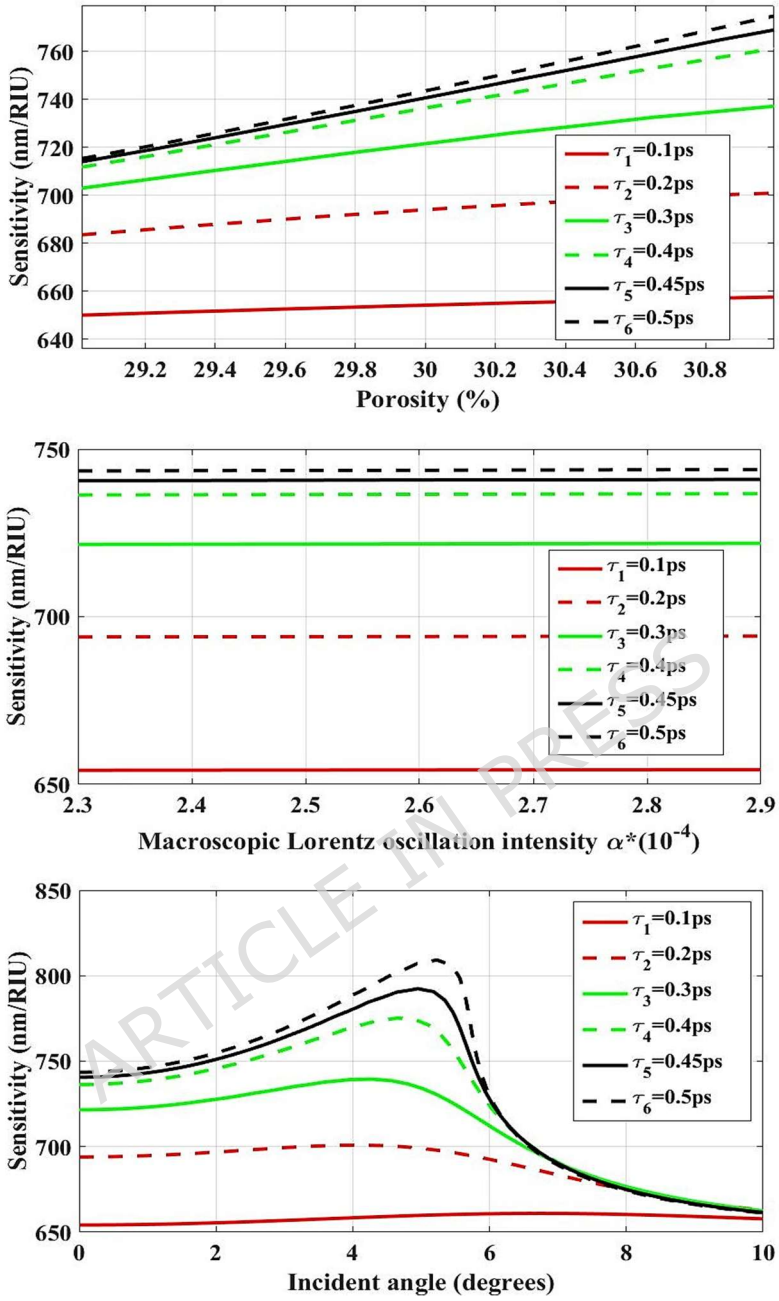

Figure 9. Sensitivity as a function of porosity (top), macroscopic Lorentz oscillation intensity (middle), and incident angle (bottom), evaluated within the tolerance range for different relaxation times.

Graphene plays a crucial role in optimizing the optical response of the proposed PT-symmetric Thue–Morse biosensor. The chemical potential directly tunes the intraband term of the Kubo conductivity, thereby strengthening the plasmonic confinement and reducing dissipative losses. Increasing μ_c sharpens the resonance, enhances the field intensity at the sensing interface, and consequently increases the refractive-index sensitivity. The relaxation time further governs the damping rate of carriers; a larger τ decreases the collision-induced absorption and leads to a substantially narrower FWHM. As a result, both higher μ_c and longer τ synergistically improve the minimum detectable wavelength shift and lower the detection limit of the sensor.

Consequently, the optimal values of the graphene chemical potential and relaxation time were determined to be 0.408 eV and 0.5 ps, respectively. Using these optimized parameters, Figures 10 and 11 shows the sensitivity and limit of detection (LoD) were evaluated for the structural configurations corresponding to Modes 2 and 4, which have two and four graphene layers in the structure, respectively.

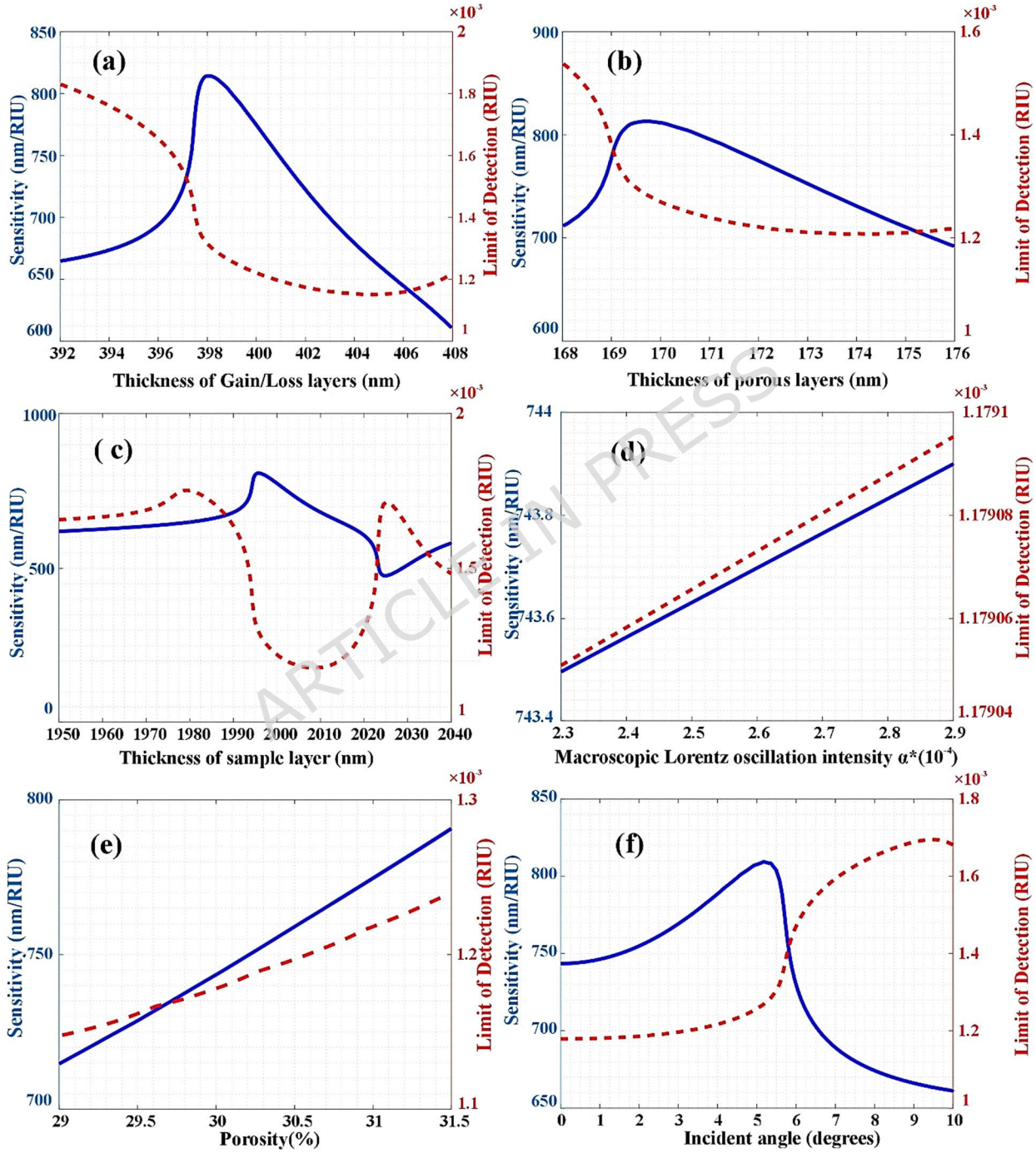

Figure 10. Sensitivity and limit of detection for mode 2, as functions of the thicknesses of the gain (loss) layers (a), porosity layers (b), and sample layer (c). The porosity (d), macroscopic Lorentz oscillation intensity (e), and incident angle (f) were evaluated within the tolerance range under optimal conditions.

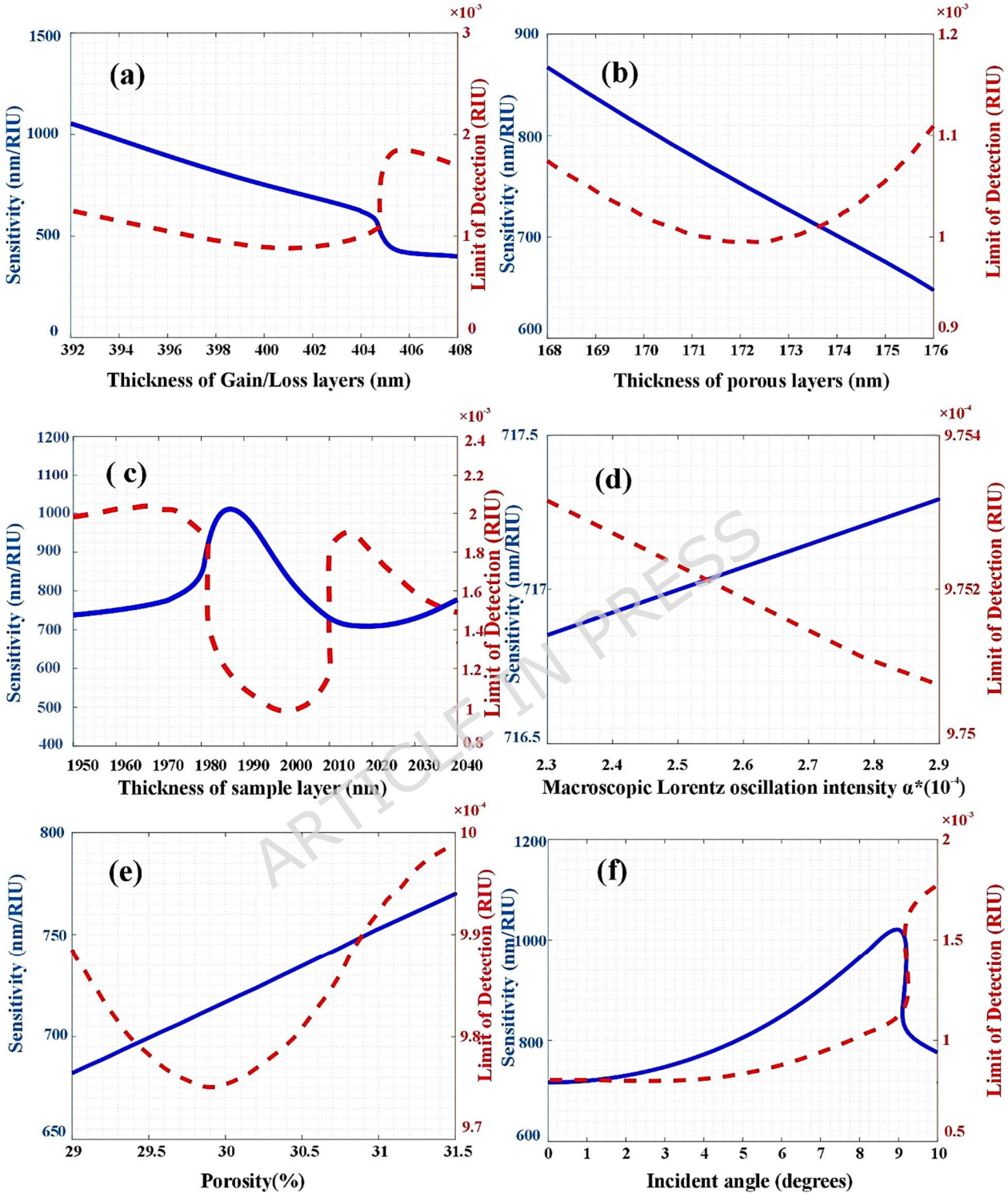

Figure 11. Sensitivity and limit of detection for mode 4, as a function of the thicknesses of the gain (loss) layers (a), porosity layers (b), and sample layer (c). The porosity (d), macroscopic Lorentz oscillation intensity (e), and incident angle (f) were evaluated within the tolerance range under optimal conditions.

The maximum sensitivity values and the corresponding minimum detection limits for the four structural modes are summarized in Table 2. In the first mode, a single graphene layer is positioned either on the left or right side of the analyte layer. The second mode corresponds to a configuration in which one graphene layer is symmetrically placed on each side of the analyte layer. The third mode, exhibiting a higher degree of asymmetry, involves two graphene layers on one side and one on the opposite side of the analyte layer. Finally, the fourth mode, which is fully symmetric and contains the most significant number of graphene layers, features two graphene sheets on each side and four in total.

Within the considered tolerance range, the optimized structural parameters of the fourth mode yield the highest sensitivity and the lowest detection limit, reaching 1054 nm/RIU and 9.875×10^{-4} RIU, respectively. It should be noted that Figures 10 and 11 illustrate the results for the second and fourth modes, while the data for the remaining configurations are presented exclusively in Table 2. Notably, the results demonstrate that increasing the number of graphene layers enhances the sensitivity while simultaneously reducing the detection limit, confirming the crucial role of graphene in improving the biosensor's performance.

Table 2. Maximum sensitivity and minimum limit of detection values of the parameters under optimal conditions.

Modes	Mode 1		Mode 2		Mode 3		Mode 4	
S &LoD Parameters (tolerance range)	**S** (nm/RIU)	**LoD** (RIU)	**S** (nm/RIU)	**LoD** (RIU)	**S** (nm/RIU)	**LoD** (RIU)	**S** (nm/RIU)	**LoD** (RIU)
$\mathbf{d_{G/L}}$(nm)	709.8 401.3	1.231×10^{-3} 406.8	812.7 397.1	1.137×10^{-3} 403.3	914.6 394.6	1.07×10^{-3} 402.7	1054 392	9.875×10^{-4} 400.9
$\mathbf{d_p}$(nm)	710 173.6	1.3×10^{-3} 174.8	810.3 168.6	1.117×10^{-3} 172.7	867 168	1.107×10^{-3} 173.4	879.7 168	9.91×10^{-4} 171.9
$\mathbf{d_s}$(nm)	713 2003	1.269×10^{-3} 2009	801.9 1994	1.115×10^{-3} 2005	910.1 1998	1.086×10^{-3} 2005	1021 1982	9.922×10^{-4} 2002
P(%)	709.1 29.92	1.241×10^{-3} 29	774.3 31	1.147×10^{-3} 29	771.1 31	1.047×10^{-3} 29	752.9 30.9	9.752×10^{-4} 29.94
$\boldsymbol{\alpha(10^{-4})}$	708.7 2.9	1.292×10^{-3} 2.3	737.1 2.9	1.179×10^{-3} 2.3	743.9 2.9	1.076×10^{-3} 2.3	771.3 2.9	9.751×10^{-4} 2.9
$\boldsymbol{\theta°}$(deg)	709.1 0	1.29×10^{-3} 0	809.3 5.175	1.179×10^{-3} 0	921.8 7.596	1.076×10^{-3} 0	1041 9.149	9.699×10^{-4} 2.261

The analysis revealed that the thickness of the gain-loss layers and the porosity of the porous silicon were the most critical parameters for maintaining sensitivity. Specifically, the optimal performance was observed when the gain-loss layers were maintained at approximately 400 nm, and the porous layers at around 30% porosity. The influence of multilayer graphene on the sensing performance was systematically examined. For few-layer graphene, the effective surface conductivity increases approximately linearly with the number of layers, which strengthens plasmonic confinement and enhances the near-field intensity at the sensing interface. This improved field localization amplifies the spectral shift induced by a small refractive-index perturbation in the analyte, thereby increasing the wavelength sensitivity. However, as the number of graphene layers where introduced by different modes increases (Modes 2 to 7, which have two to seven graphene layers in the structure), absorption losses also grow, leading to broader resonance features (higher FWHM) and reduced resonance depth. Consequently, an optimal number of graphene layers exists that balances enhanced sensitivity with acceptable resonance quality. To identify this optimum, parameter sweeps were performed over the number of graphene layers and the gain/loss layer thickness and the porosity. The optimal configuration was determined by maximizing the sensitivity (equivalently minimizing the LoD), while ensuring sufficient resonance contrast and practical fabrication constraints. Our results show that, for realistic material parameters, the highest sensitivity is achieved for mode 4 with four graphene layers, together with the gain/loss thicknesses and porosity values reported in Figs. 12 to 15. Beyond this point, the marginal increase in sensitivity is outweighed by stronger absorption and an increase in FWHM, which degrades the overall sensing performance. We therefore conclude that a four-layer graphene coating as mode 4, provides the optimum performance for the proposed Thue–Morse–based biosensor as listed in Tables 3 and 4.

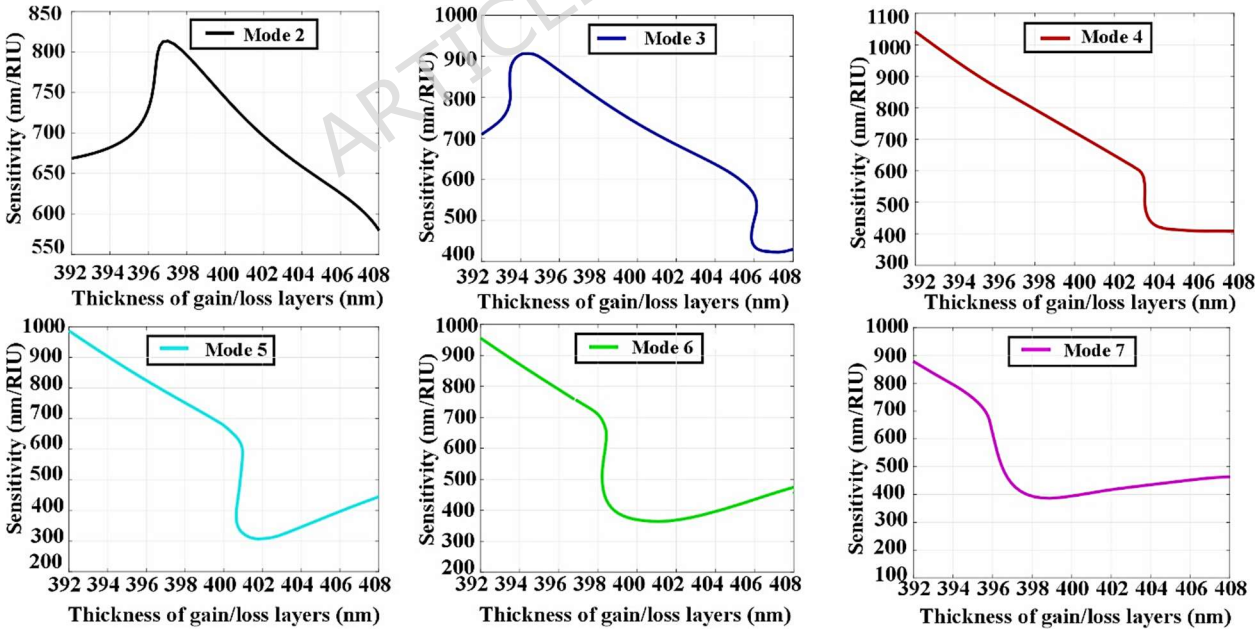

Figure 12. Sensitivity for different modes as a function of the gain/loss layer thicknesses, evaluated within the ±2% fabrication tolerance range under optimal operating conditions.

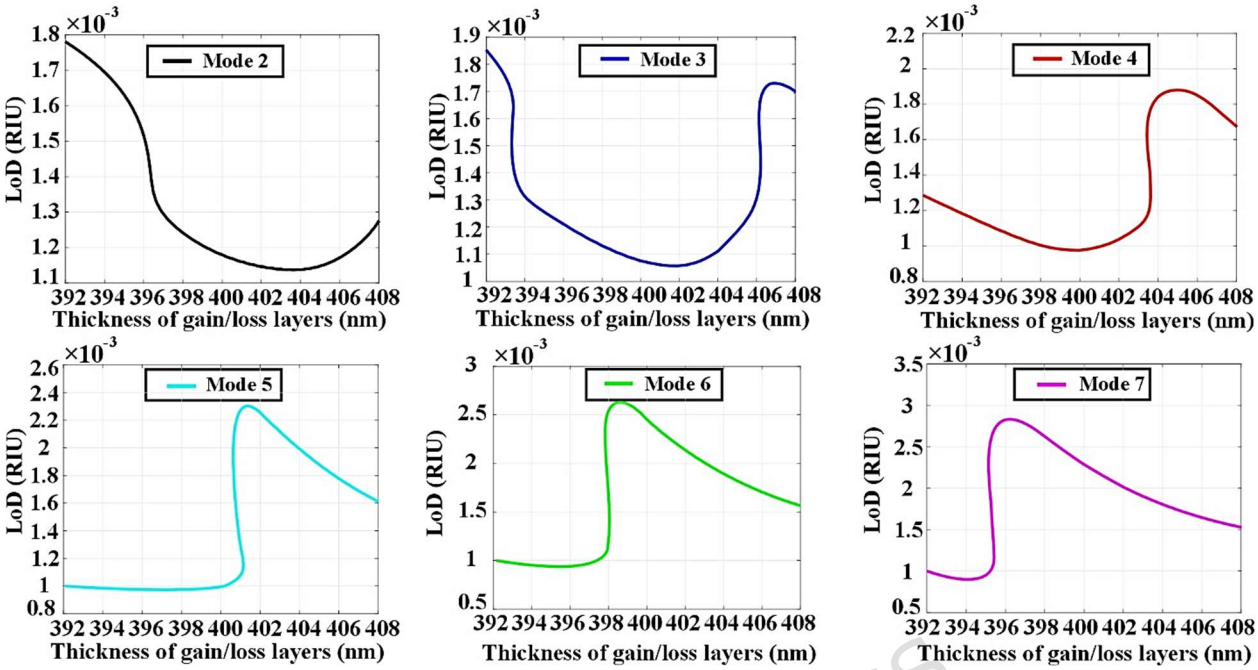

Figure 13. Limit of detection for different modes as a function of the gain/loss layer thicknesses, evaluated within the ±2% fabrication tolerance range under optimal operating conditions.

Table 3. Sensitivity and limit of detection values for different modes as a function of the gain/loss layer thickness.

Modes	Mode 2	Mode 3	Mode 4	Mode 5	Mode 6	Mode 7
Sensitivity (nm/RIU)	812.7	914.6	1054	989.2	948.3	881
LoD (RIU)	1.137×10^{-3}	1.107×10^{-3}	9.875×10^{-4}	9.889×10^{-4}	9.878×10^{-4}	9.831×10^{-4}

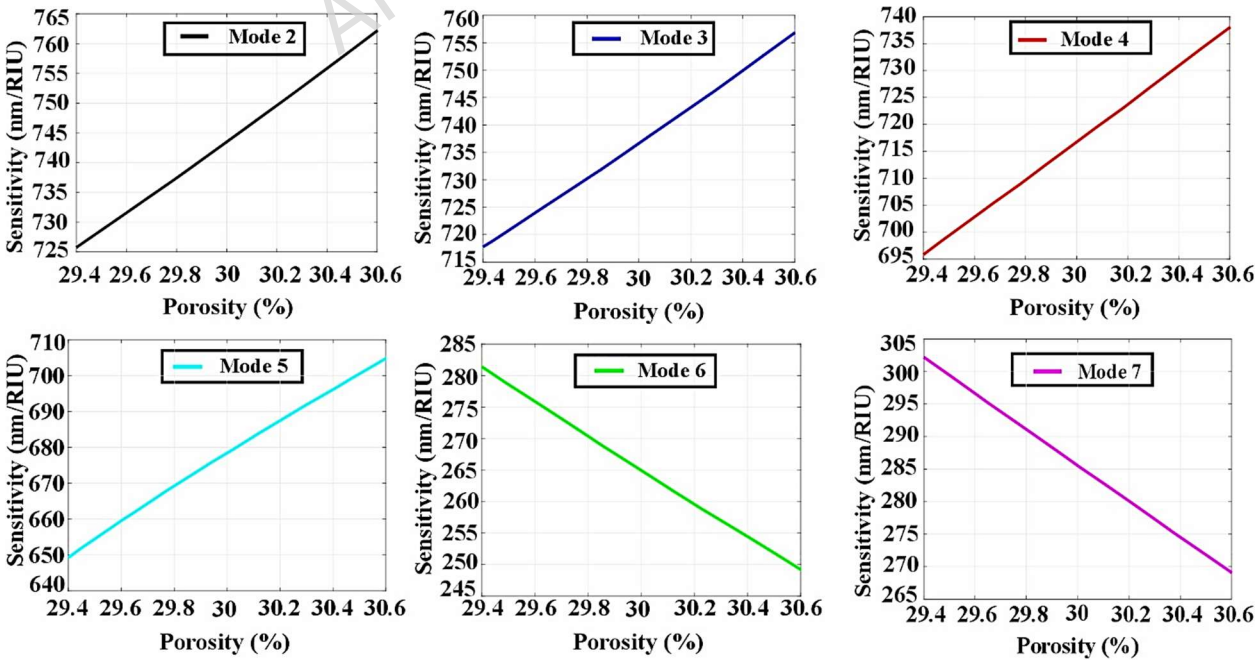

Figure 14. Sensitivity for different modes as a function of the porosity, evaluated within the ±2% fabrication tolerance range under optimal operating conditions.

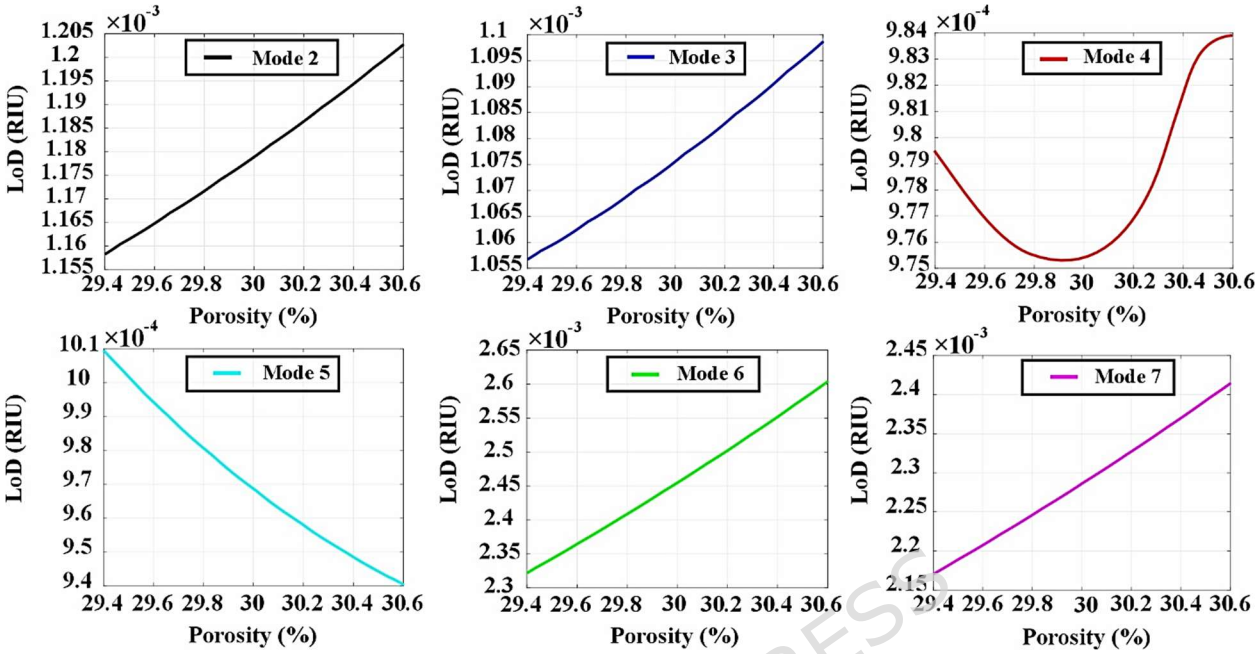

Figure 15. Limit of detection for different modes as a function of the porosity, evaluated within the ±2% fabrication tolerance range under optimal operating conditions.

Table 4. Sensitivity and limit of detection values for different modes as a function of the porosity.

Modes	Mode 2	Mode 3	Mode 4	Mode 5	Mode 6	Mode 7
Sensitivity (nm/RIU)	762	751.3	737.8	704.2	281.4	302
LoD (RIU)	1.158×10^{-3}	1.057×10^{-3}	9.752×10^{-4}	9.41×10^{-4}	2.325×10^{-3}	2.17×10^{-3}

A comparison with values reported in previous studies is presented in Table 5, which demonstrates that the results obtained here are more favourable, particularly due to the incorporation of the graphene layer into the structure. As shown in Table 5, many 1D photonic biosensors achieve sensitivities from ~100 nm/RIU up to several hundred nm/RIU, and LoDs ranging from 10^{-3} to 10^{-6} RIU in simulation or specialized fiber systems. Our device, is less competitive in absolute LoD compared to fiber-based or idealized designs, but its major advantage lies in its miniaturized PT-symmetric graphene architecture which may offer robustness, integrability, and ease of fabrication. Graphene offers electrically tunable optical conductivity, reduced plasmonic damping, and stronger near-field localization. These features allow the proposed structure to achieve sharper resonances, enhanced interaction with the analyte layer, and sensitivity levels that cannot be realized in metal-based PRISM configurations. Furthermore, the combination of graphene tunability with PT-symmetric EP engineering provides access to ultrasteep spectral slopes and significantly improves the overall sensing performance.

Table 5. Comparison of 1D photonic biosensor / refractive-index sensors.

Structure/Configuration	Sensitivity (nm/RIU)	LoD(RIU)	Reference	Year
A resonant mode effect of 1D PhC for the detection of cancer cells	43	NC*	Ramanujam et al. [36]	2018
A protein sensor based on a 1D PhC with a central defect	170	NC	Aziz et al. [37]	2019
A gas sensor operated in IR regime by using a PhC with point defect	270	$\square 10^{-4}$	Baghdouche et al. [38]	2020
A blood hemoglobin sensor with a defect mode	167	NC	Abdla et al. [39]	2020
Defective 1D PhC with a defect cavity	102	3.50×10^{-5}	Aly et al. [40]	2021
A blood plasma and cancer cell sensor by employing a 1D PhC structure	73	NC	Bijalwan et al. [24]	2021
1D defective PhC with graphene	290	NC	Panda et al. [25]	2021
1D PT-symmetric PhC with a central defect layer	227	5.10×10^{-6}	Yi et al. [23]	2021
A defective PhC waveguide for cancerous blood detection	344	NC	Abohassan et al. [41]	2021
Nonlinear delta-function PhC for detecting sodium iodide solution	410	8.00×10^{-4}	Mehaney et al. [42]	2022
1D PhC (metal + cavity + periodic dielectric) with Hybrid Tamm plasmon	259	NC	Jena et al. [43]	2022
1D PhC of ZnSe/Nb2O5/BK7 as a tunable wide bandstop filter	81	90.00×10^{-6}	Abohassan et al. [44]	2022
1D multilayer PhC with defect (bio-alcohol sensor)	500	1×10^{-5}	Al-Dossari et al. [45]	2022
1D quasi-PT symmetric photonic biosensor	635	1.20×10^{-3}	Zaky et al. [21]	2022
1D defect-layer PhC (DLPhC)	650	NC	Sampath et al. [46]	2024
Supercell-based plasmonic metamaterials	604	3.40×10^{-3}	Faraji et al. [47]	2025
1D miniaturized augmented PT symmetric photonic biosensor	413	6.31×10^{-5}	Mohammadpour et al. [48]	2025
1D PT symmetric Thue-Morse photonic biosensor with graphene	1054	9.875×10^{-4}	**This work**	

*NC→ No calculated.

As summarized in Table 5, the proposed Thue–Morse PT-symmetric graphene-enhanced biosensor outperforms most previously reported PT-symmetric or graphene-assisted plasmonic platforms in terms of wavelength sensitivity and achievable detection limit. Conventional PT-symmetric sensors typically rely on periodic multilayer structures, which offer enhanced spectral response but often suffer from limited field localization and moderately broad resonances. Similarly, graphene-based SPR configurations reported in the literature generally achieve improved tunability but remain constrained by plasmonic damping in metallic components and the absence of exceptional-point–induced resonance sharpening. In contrast, our design benefits simultaneously from quasi-periodic Thue–Morse engineering which strengthens mode localization and suppresses disorder-induced broadening and from PT-symmetry breaking at an exceptional point, which produces an ultrasteep spectral slope. Combined with graphene supporting strong and tunable surface conductivity, the resulting hybrid structure provides substantially higher field enhancement within the analyte region. This explains why the proposed device achieves sensitivity

values exceeding 1000 nm/RIU and detection limits on the order of 10^{-4} RIU, significantly lower than previously reported PT-symmetric or graphene-plasmonic biosensors.

Despite the strong performance, the proposed architecture also presents several practical limitations. First, exploiting the exceptional point requires precise balancing of gain–loss and accurate control of layer thicknesses in the Thue–Morse sequence; thus, fabrication tolerances tighter than those typically required for periodic photonic crystals may be necessary. Second, while increasing the number of graphene layers enhances plasmonic confinement and boosts sensitivity, it also increases absorption and imposes stricter requirements on graphene transfer quality and interface smoothness. Thus, a trade-off exists between maximizing sensitivity and maintaining low optical loss and feasible fabrication. Third, the quasi-periodic nature of the structure, although beneficial for field localization, increases the total number of layers, thereby adding complexity compared to simpler periodic PT-symmetric stacks. These considerations highlight that the superior performance of the proposed sensor stems from a careful balance of quasi-periodicity, PT-symmetry, and graphene-induced tunability, but also that practical fabrication constraints should be taken into account in future experimental realizations.

The analysis confirms that the biosensor maintains stable performance under realistic fabrication tolerances, demonstrating a balance between sensitivity enhancement and practical feasibility for experimental implementations. The surface of the porous silicon and graphene layers can be functionalized with specific antibodies or biomolecules that selectively bind to different cancer biomarkers. This functionalization enables the biosensor to target a wide array of biomarkers relevant to specific cancer types, facilitating personalized diagnostics. By designing the sensor to accommodate multiple analyte layers or by employing spatially multiplexed sensing techniques, the biosensor can simultaneously detect multiple cancer biomarkers in a single assay. This capability enhances the efficiency and speed of diagnostics in clinical settings. Incorporating microfluidic systems allows for continuous flow analysis of liquid biopsies, such as blood or saliva samples. This integration can automate the sampling process, enabling real-time monitoring of biomarker levels, which is crucial for dynamic cancer diagnostics. The sensor's ability to provide real-time optical readouts allows for immediate assessment of biomarker concentrations as samples are introduced. The sensitivity to refractive index changes ensures that even low-abundance biomarkers can be detected, making it suitable for early cancer detection. Ongoing research into optimizing the chemical potential and relaxation time of graphene, along with the design of gain-loss layers, can further enhance sensitivity and selectivity, enabling detection of low-affinity biomarker interactions common in cancer diagnostics.

Fabrication considerations and practical feasibility

Although the tolerance analysis demonstrates that the proposed design is robust against ±2% variations in structural parameters, it is important to acknowledge several practical considerations relevant to fabrication. Integrating graphene layers and gain media within a porous silicon platform can be challenging because porous silicon naturally exhibits surface roughness and a highly textured internal structure. These properties may influence the uniformity of transferred graphene films and the distribution of infiltrated gain materials. Nevertheless, a number of recent studies have demonstrated the feasibility of depositing few-layer graphene on porous substrates and

incorporating dye-based or rare-earth–based gain materials into porous silicon matrices. These reports indicate that, although careful process optimization is required, the fabrication steps needed for our design lie within the capabilities of current nanofabrication and material-transfer techniques. To support potential experimental implementation, we note that practical fabrication would likely involve three general steps: (i) forming the porous silicon layers with controlled porosity and thickness, (ii) transferring graphene layers using established large-area transfer approaches, and (iii) infiltrating the gain medium through capillary-assisted filling. Each of these steps has already been demonstrated in related photonic structures, suggesting that the proposed architecture is experimentally attainable with reasonable process refinement.

4. Conclusion

In this work, we proposed and systematically analyzed a one-dimensional Thue–Morse photonic crystal biosensor that exploits parity–time (PT) symmetry and exceptional point (EP) physics, with optional graphene integration, for the sensitive detection of cancerous and healthy tissue samples. By combining quasi-periodic ordering, porous silicon layers, and carefully engineered gain–loss distributions, the device supports sharp defect-mode resonances whose response is strongly amplified in the vicinity of EPs. The incorporation of graphene nanolayers further enhances light–matter interaction, enabling significant improvements in spectral sensitivity and detection capability. Through parametric optimization, **the chemical potential** and **relaxation time** of graphene were identified as **0.408 eV** and **0.5 ps**, respectively. Under these optimized conditions, the biosensor demonstrated a **maximum sensitivity of 1054 nm/RIU** with a corresponding **detection limit of 9.875×10^{-4} RIU**. These values are superior to those reported for many conventional one-dimensional photonic biosensors, highlighting the benefits of the synergistic integration of EP engineering, Thue–Morse ordering, and graphene-assisted field confinement. The analysis of fabrication tolerances confirmed that the proposed architecture maintains stable performance within realistic variations of structural parameters, underscoring its robustness and potential for experimental implementation. Compared to previously reported designs, the present configuration offers a compelling balance of miniaturization, high sensitivity, and practical feasibility. Overall, the results demonstrate that graphene-enhanced PT-symmetric Thue–Morse photonic crystals represent a powerful platform for next-generation optical biosensors. The approach provides a pathway to robust, label-free, and high-sensitivity detection of cancer cells and tissues, and may be extended to other biomedical analytes and diagnostic applications. Future work could explore experimental fabrication, integration with microfluidic systems, and further optimization for multiplexed detection schemes.

Data availability

The datasets generated and/or analyzed during the current study are available from the corresponding author upon reasonable request.

References

[1] B. Kaur, S. Kumar and B. K. Kaushik, "Recent advancements in optical biosensors for cancer detection," *Biosensors and Bioelectronics,* vol. 113805, no. 197, 2022.

[2] J. L. Santos and F. Farahi, Handbook of Optical Sensors, CRC Press, 2015.

[3] A. Ramola, A. K. Shakya, A. Droby and A. Bergman, "Numerical Study of a Novel Kagome-Inspired Photonic Crystal Fiber-Based Surface Plasmon Resonance Biosensor for Detection of Blood Components and Analytical Targets," *Biosensors,* vol. 15, no. 539, 2025.

[4] A. Ramola, A. K. Shakya, V. Kumar and A. Bergman, "Recent Advances in Photonic Crystal Fiber-Based SPR Biosensors: Design Strategies, Plasmonic Materials, and Applications," *Micromachines,* vol. 16, no. 747, 2025.

[5] A. Ramola, A. K. Shakya and A. Bergman, "Finite Element Method-Based Modeling of a Novel Square Photonic Crystal Fiber Surface Plasmon Resonance Sensor with a Au–TiO2 Interface and the Relevance of Artificial Intelligence Techniques in Sensor Optimization," *Photonics,* vol. 12, no. 565, 2025.

[6] A. Ramola, A. K. Shakya and A. Bergman, "Comprehensive Analysis of Advancement in Optical Biosensing Techniques for Early Detection of Cancerous Cells," *Biosensors,* vol. 15, no. 292, 2025.

[7] A. K. Shakya and S. Singh, "Development of a generalized Fourier transform model for distinct household oil samples by performing spectroscopy analysis," *Results in Optics,* vol. 10, no. 100355, 2023.

[8] A. Ramola, A. K. Shakya, A. Vidyarthi, S. Singh, E. Talker and A. Bergman, "Next-generation photonic-crystal-fiber-based plasmonic sensor for heavy metal detection via spectroscopy and refractive index integration," in *29th International Conference on Optical Fiber Sensors*, Porto, Portugal, 2025.

[9] A. Krasnok, N. Nefedkin and A. Alu, "Parity-Time Symmetry and Exceptional Points," *IEEE Antennas & Propagation Magazine,* vol. 63, no. 6, 2021.

[10] A. Mohammadpour, J. Barvestani and A. S. Vala, "Extraordinary directional optical properties of a parity-time symmetric one-dimensional photonic lattice," *Opt. Commun.,* vol. 500, no. 127342, 2021.

[11] R. Duggan, S. A. Mann and A. Alu, "Limitations of Sensing at an Exceptional Point," *ACS Photonics,* vol. 9, pp. 1554-1566, 2022.

[12] L. Moretti, I. Rea, L. Rotiroti, I. Rendina, G. Abbate, A. Marino and L. D. Stefano, "Photonic band gaps analysis of Thue-Morse multilayers made of porous silicon," *Opt. Express,* vol. 14(13), pp. 6264-72, 2006.

[13] A. Mohammadpour, J. Barvestani and A. S. Vala, "Comprehensive study of singular points in a PT-symmetric Thue-Morse multilayer," *Physica Scripta,* vol. 97, no. 125501, 2022.

[14] A. M. Abd-Elnaiem, Z. E. A. Mohamed, S. Elshahat, M. Almokhtar and M. Norek, "Recent Progress in the Fabrication of Photonic Crystals Based on Porous Anodic Materials," *Energies,* vol. 16(10), no. 4032, 2023.

[15] C. Pacholski, "Photonic crystal sensors based on porous silicon," *Sensors,* vol. 13(4), no. 4694, 2013.

[16] L. Canham, Handbook of Porous Silicon, Springer, 2020.

[17] A. Jane, R. Dronov, A. Hodges and N. H. Voelcker, "Porous silicon biosensors on the advance," *Trends Biotechnol.,* vol. 27(4), pp. 230-9, 2009.

[18] H. K. Baghbadorani, J. Barvestani and S. R. Entezar, "Biosensors based on Bloch surface waves in one-dimensional photonic crystal with graphene nanolayers," *Appl Opt,* vol. 56(3), pp. 462-469, 2017.

[19] X. Bo, M. Zhou and L. Guo, "Electrochemical sensors and biosensors based on less aggregated graphene," *Biosens Bioelectron,* vol. 89, pp. 167-186, 2017.

[20] A. H. Aly and Z. A. Zaky, "Ultra-sensitive photonic crystal cancer cells sensor with a high-quality factor," *Cryogenics,* vol. 104, no. 102991, 2019.

[21] Z. A. Zaky, S. Alamri, V. D. Zhaketov and A. H. Aly, "Refractive index sensor with magnified resonant signal," *Sci. Rep.,* vol. 12, no. 1377, 2022.

[22] N. A. Vanyushkin, I. M. Efimov and A. H. Gevorgyan, "The sensitivity of refractive index sensors based on defected 1D photonic crystals: an analytical approach," *Phys. Scr.,* vol. 99, no. 105521, 2024.

[23] L. Yi and C. Li, "Simulation Research on Blood Detection Sensing with Parity-Time Symmetry Structure," *Crystals,* vol. 11, no. 1030, 2021.

[24] A. Bijalwan, B. K. Singh and V. Rastogi, "Analysis of one-dimensional photonic crystal based sensor for detection of blood plasma and cancer cells," *Optik,* vol. 226, no. 165994, 2021.

[25] A. Panda, P. D. Pukhrambam, F. Wu and W. Belhadj, "Graphene-based 1D defective photonic crystal biosensor for real-time detection of cancer cells," *Eur. Phys. J. Plus,* vol. 136, no. 809, 2021.

[26] M. F. Nayan, M. A. Raihan, M. H. Fuad, N. A. Zaman, T. Ahmed and R. R. Mahmud, "A high-performance biosensor based on one-dimensional photonic crystal for the detection of cancer cells," *Optical and Quantum Electronics ,* vol. 56, no. 1968, 2024.

[27] Z. A. Zaky, M. Al-Dossari, A. Sharma and A. H. Aly, "Effective pressure sensor using the parity-time symmetric photonic crystal," *Physica Scripta,* vol. 98, no. 035522, 2023.

[28] M. Kolar, M. K. Ali and E. Nori, "Generalized Thue-Morse chains and their physical properties," *Phys. Rev. B,* vol. 43, no. 1, 1991.

[29] K. Ziegler, "Minimal conductivity of graphene: Nonuniversal values from the Kubo formula," *Phys. Rev. B,* vol. 75, no. 233407, 2007.

[30] J. Barvestani and A. Mohammadpour, "The effect of the centric graphene layer on the exceptional points of parity-time symmetric photonic crystals," *Optical and Quantum Electronics,* vol. 56, no. 880, 2024.

[31] T. G. Mackay and A. Lakhtakia, The transfer matrix method in electromagnetics and optics, Morgan & Claypool, 2020.

[32] A. Doval, C. D. Rodríguez-Fernández, H. González-Núñez and R. d. l. Fuente, "Fresnel coefficients, coherent optical scattering, and planar waveguiding," *Physica Scripta,* vol. 99, no. 026101, 2024.

[33] J. Barvestani and A. Mohammadpour, "Tunable and giant spatial Goos–Hänchen shifts in a parity-time symmetric Cantor photonic crystals incorporated with a centered graphene layer," *Physica Scripta,* vol. 98, no. 055511, 2023.

[34] V. Klimov, A. Mikhailovsky, S. Xue, A. Malko, J. Hollingsworth, C. Leatherdale, H. Eisler and M. Bawendi, "Optical Gain and Stimulated Emission in Nanocrystal Quantum Dots," *Science,* vol. 290, no. 314, 2000.

[35] J. Homola, "Surface plasmon resonance sensors for detection of chemical and biological species," *Chemical Reviews,* vol. 108(2), pp. 462-493, 2008.

[36] N. R. Ramanujam, I. S. Amiri, S. A. Taya, S. Olyaee, R. Udaiyakumar, A. P. Pandian, K. S. J. Wilson, P. Mahalakshmi and P. P. Yupapin, "Enhanced sensitivity of cancer cell using one dimensional nano composite material coated photonic crystal," *Microsystem Technologies,* 2018.

[37] O. A. A. El-Aziz, H. A. Elsayed and M. I. Sayed, "One-dimensional defective photonic crystals for the sensing and detection of protein," *Appl. Opt.,* vol. 58(30), pp. 8309-8315, 2019.

[38] L. Kassa-Baghdouche and E. Cassan, "Mid-infrared gas sensor based on high-Q/V point-defect photonic crystal nanocavities," *Opt. Quantum Electron.,* vol. 52, 2020.

[39] M. M. Abadla and H. A. Elsayed, "Detection and sensing of hemoglobin using one-dimensional binary photonic crystals comprising a defect layer," *Appl. Opt.,* vol. 59(2), pp. 418-424, 2020.

[40] A. H. Aly, S. K. Awasthi, D. Mohamed, Z. S. Matar, M. Al-Dossari and A. F. Amin, "Study on a one-dimensional defective photonic crystal suitable for organic compound sensing applications," *RSC Adv.,* vol. 11(52), pp. 32973-32980, 2021.

[41] K. M. Abohassan, H. S. Ashour and M. M. Abadla, "A 1D photonic crystal-based sensor for detection of cancerous blood cells," *Opt. Quantum Electron.,* vol. 53, pp. 1-14, 2021.

[42] A. Mehaney, M. M. Abadla and H. A. Elsayed, "Biosensors based on novel nonlinear delta-function photonic crystal comprising weak nonlinearities," *Sci. Reports,* vol. 12, no. 17674, 2022.

[43] S. Jena, R. B. Tokas, S. Thakur and D. V. Udupa, "Rabi-like splitting and refractive index sensing with hybrid Tamm plasmon-cavity modes," *J. Phys. D: Appl. Phys.,* vol. 55, no. 175104, 2022.

[44] K. M. Abohassan, H. S. Ashour and M. M. Abadla, "Tunable wide bandstop and narrow bandpass filters based on one-dimensional ternary photonic crystals comprising defects of silver nanoparticles in water," *J. Phys. Chem. Solids,* vol. 161, no. 110484, 2022.

[45] M. Al-Dossari, S. K. Awasthi, A. M. Mohamed, N. S. A. El-Gawaad, W. Sabra and A. H. Aly, "Bio-Alcohol Sensor Based on One-Dimensional Photonic Crystals for Detection of Organic Materials in Wastewater," *Materials,* vol. 15(11), no. 4012, 2022.

[46] D. Sampath and V. Narasimhan, "One-Dimensional Defect Layer Photonic Crystal Sensor for Purity Assessment of Organic Solvents," *ACS Omega,* vol. 9, no. 8, 2024.

[47] M. Faraji, A. Jangjoy and S. Matloub, "Octa- square split ring-shaped supercell-based plasmonic metamaterials for enhanced dual-spectral detection of cancer biomarkers," *Sci. Reports,* vol. 15, no. 33136, 2025.

[48] A. Mohammadpour, A. S. Vala and J. Barvestani, "Sensitive Detection of Cancer and Brain Tissues Using a Miniaturized PT-Symmetric Nanophotonic Biosensor Based on Exceptional Points," *Sci. Reports,* Online First, https://doi.org/10.1038/s41598-025-30897-3, 2025.

Acknowledgments

This work is based upon research funded by Iran National Science Foundation (INSF) and Supreme Council of Science, Research and Technology (SCSRT) under project No. 4023866.

Funding

This work is based upon research funded by Iran National Science Foundation (INSF) and Supreme Council of Science, Research and Technology (SCSRT) under project No. 4023866.

Author contributions

A.M. conceived the research idea, performed the computational analysis, interpreted the results, and wrote the manuscript. A.M., A.S.V., and J.B. reviewed and edited the manuscript. All authors read and approved the final version of the manuscript.

Competing interests

The authors declare that they have no known competing financial interests or personal relationships that could have appeared to influence the work reported in this paper.

Additional information

Correspondence and requests for materials should be addressed to A.M.